Journal of Materials Chemistry A

ROYAL SOCIETY OF CHEMISTRY

PAPER

View Article Online
View Journal

Cite this: DOI: 10.1039/d5ta10187e

Selection of a single atom for surface charge modulation to promote CO_2 activation and stabilize the *COOH intermediate for solar fuels

Chih-Yang Huang,[abc] Ying-Ren Lai,[cd] Yi-Fan Huang,[e] Tsai-Yu Lin,[abc] Kongpop Limwatcharagul,[abc] Mengstu Etay Ashebir,[cfghi] Heng-Liang Wu,[cdj] Michitoshi Hayashi,*[cd] Mohammad Qorbani,*[kl] Kuei-Hsien Chen*[ci] and Li-Chyong Chen*[cdm]

Modulating the surface charge distribution is a key strategy for enhancing photocatalytic CO_2 reduction as it effectively activates the inert CO_2 molecule into a reactive, bent configuration. However, the rational design of such catalysts is fundamentally challenged by the lack of a systematic, predictive guideline for selecting optimally anchored single-metal atoms. We address this critical gap by establishing a novel predictive metal selection principle based on the synergistic effect of the valence electron count and electronegativity of a single atom. This principle successfully guided the selection of transition metals (Cr, Fe, and Ni) anchored onto WO_3 nanoplates *via* wet impregnation, ensuring selective surface modification while preserving the bulk properties. The Fe-anchored WO_3 catalyst, identified by our principle, demonstrated the most substantial surface electron density localization. This rational optimization led to a remarkable three-fold enhancement in the PC-CO_2RR efficiency, selectively yielding CO as the primary product. Comprehensive experimental and theoretical analyses confirmed that this localized charge accumulation promotes significantly stronger CO_2 chemisorption and critically stabilizes the key intermediate, *COOH. Specifically, the reaction became thermodynamically spontaneous with ΔG(*COOH) = −1.73 eV. Our findings establish a strong correlation between the localized surface charge density and CO_2 activation, providing a fundamental and generalizable guideline for the rational design of high-performance catalytic materials for energy and sustainability applications.

Received 13th December 2025
Accepted 14th April 2026

DOI: 10.1039/d5ta10187e

rsc.li/materials-a

1 Introduction

Global warming has been a concern for several decades, leading to serious environmental problems, such as rising mean surface temperature and sea levels and climate change.[1] In particular, carbon dioxide (CO_2) is one of the most threatening greenhouse gases due to its massive emissions from human activities, which may cause serious or irreversible damage.[2] As one of the alternative solutions, the photocatalytic CO_2 reduction reaction (PC-CO_2RR) has attracted research attention as it can convert CO_2 into valuable fuels (such as CO and CH_4) using sustainable solar energy.[3–6] However, the PC-CO_2RR is limited by its low conversion efficiency due to the chemically inert nature of the linear configuration of the CO_2 molecule.[7] According to the literature, the adsorption of CO_2 on surface active sites is a critical step and plays a significant role in influencing the reduction reaction pathways and ultimately determining the productivity and selectivity of PC processes.[3,8] While intrinsic defects, grain boundaries, and edges are recognized as active sites for the CO_2RR, activating CO_2 on the inert basal plane or the surface atomic structure of the catalyst is more advantageous.[9–11] Therefore, redesigning the surface of

[a]International Graduate Program of Molecular Science and Technology, National Taiwan University (NTU-MST), Taipei 10617, Taiwan
[b]Molecular Science and Technology Program, Taiwan International Graduate Program (TIGP), Academia Sinica, Taipei 11529, Taiwan
[c]Center for Condensed Matter Sciences, National Taiwan University, Taipei 10617, Taiwan. E-mail: chenkh@pub.iams.sinica.edu.tw; chenlc@ntu.edu.tw
[d]Center of Atomic Initiative for New Materials, National Taiwan University, Taipei, 10617, Taiwan
[e]Department of Mechanical Engineering, National Chin-Yi University of Technology, Taichung 411030, Taiwan
[f]Sustainable Chemical Science and Technology, Taiwan International Graduate Program, Academia Sinica, Nankang, Taipei 11529, Taiwan
[g]Institute of Chemistry, Academia Sinica, Nankang, Taipei 11529, Taiwan
[h]Department of Applied Chemistry, National Yang Ming Chiao Tung University, Hsinchu, 30010, Taiwan
[i]Institute of Atomic and Molecular Sciences, Academia Sinica, Taipei 10617, Taiwan
[j]Department of Chemistry, National Taiwan University, Taipei 10617, Taiwan
[k]Undergraduate Program of Electro-Optical Engineering, National Taiwan Normal University, Taipei 11677, Taiwan. E-mail: qorbani@ntnu.edu.tw
[l]Institute of Electro-Optical Engineering, National Taiwan Normal University, Taipei 11677, Taiwan
[m]Department of Physics, National Taiwan University, Taipei 10617, Taiwan

a catalyst to enhance the product yield is essential for achieving high conversion efficiency.

In the realm of photocatalysis, the arrangement of atoms on the catalyst surface is momentous due to its substantial impact on the surface electron density distribution for catalytic activity and selectivity.[12–14] For instance, charge-enriched dual metal site catalysts, *e.g.*, V_S–$CuIn_5S_8$, alter the CO_2 adsorption mode from weak M–C or M–O bonds to stronger M–C–O–M bonds. This alteration allows CO_2 to remain on the catalyst surface for a longer duration, awaiting the subsequent protonation step, all the way to yield CH_4.[12] Generally, the localized surface electron density enables CO_2 adsorption through orbital hybridization between C or O and surface atoms.[13,15,16] Several studies have focused on surface engineering to modify the surface atomic structure to enhance the efficiency of the PC-CO_2RR.[13,15–17] For example, Zhou and coworkers manipulated charge accumulation by anchoring Au single atoms and regulating the vacancy types in the host material. As a result, CO_2 interaction with the catalyst surface changed from physical to chemical adsorption.[13] The chemisorption of CO_2 on the catalyst surface leads to electron transfer from the catalyst to the antibonding orbitals of CO_2, which weakens the C=O bonds and facilitates subsequent chemical transformations.[18] This structural change converts CO_2 to a nucleophilic species, leading to the easier activation of CO_2 for photocatalytic conversion.[18–20]

To achieve surface charge accumulation, doping engineering is the most effective method.[21–24] However, conventional doping methods, such as one-pot synthesis, may not be ideal because they can alter the entire crystal structure of the catalyst, which may potentially introduce detrimental defects and cause significant carrier recombination.[25–27] In contrast, the wet impregnation approach enables selective modification of surface properties by anchoring dopants on the host semiconducting material without affecting its bulk characteristics.[25,28] Hence, anchored dopants can function as supplementary catalytically active sites directly at the surface-ambient interface.[28–30]

Currently, single-atom catalysts (SACs) have garnered immense interest due to their exceptional ability to significantly boost catalytic performance even at minimal metal loadings. Beyond merely enhancing physical properties, such as light absorption and charge transfer and separation, and introducing new active sites,[31,32] recent studies have highlighted that these improvements fundamentally stem from the precise control of electronic structures.[33] SACs enable the strategic regulation of orbital electron occupancy in adsorbates, thereby stabilizing specific key intermediates.[34,35] Consequently, research has begun to focus on dual or multi-single-atom systems to steer product selectivity from C1 to C2 products.[36,37] By manipulating surface charge populations, it is possible to finely tune adsorption strength and intermediate stability, which is a vital consideration for the future development of multicarbon fuels.

However, a significant challenge remains: the selection of the optimal transition metal atom for anchoring lacks a systematic, predictable guideline. Existing studies often rely on trial-and-error, limiting the efficient, rational design of advanced catalysts. This limitation is particularly evident in the sparse exploration of spin effects on the occupancy of antibonding orbitals within key intermediates. Such electronic regulation is essential for optimizing the electronic acceptance–donation interaction between the catalyst and reactants, as recent studies suggest that spin-polarized states can significantly stabilize intermediate species through d-orbital rearrangement.[34,35] Addressing this crucial gap, our study establishes a clear selection mechanism. We propose that the key to maximizing electron enrichment on the model catalyst surface lies in the synergistic effect of the number of valence electrons of the metal and its electronegativity. This principle allows us to predictively select single transition metal atoms that can induce the strongest localized charge accumulation, optimizing CO_2 activation. Ultimately, the electronegativity and valence electron count can serve as robust descriptors to predict and guide the selection of suitable transition metals, thereby laying a foundational framework for the rational design of high-performance catalytic materials.

Inspired by the above statements, we designed a series of transition metal-anchored WO_3 catalysts to enhance CO_2 adsorption and promote CO_2 reduction. Notably, WO_3 nanoplates were selected as the model catalyst due to their earth-abundance, economical cost, nontoxicity, and photostability.[38,39] The wet impregnation method was employed to selectively introduce fourth-period transition metals (Cr, Fe, and Ni) as anchored dopants on the surface of WO_3. These elements were selected due to their excellent catalytic performance and their capability to effectively modulate surface charge density.[21,40,41] Characterization techniques, including X-ray absorption near-edge structure (XANES), X-ray photoelectron spectroscopy (XPS), *in situ* Fourier transform infrared (FTIR) spectroscopy, and density functional theory (DFT) calculations, revealed modulation of the charge density distribution and *COOH key intermediate stabilization; asterisks stand for the active site when transition metals are anchored on the surface. The enhancements in CO_2 adsorption and activation were also proven through theoretical calculations and the experimental PC-CO_2RR. Ultimately, a strong correlation between charge accumulation, CO_2 adsorption, and activation was observed, providing valuable insights for the design of next-generation catalysts.

2 Experimental

2.1 Chemicals

All chemicals and reagents were of analytical grade and used directly without further purification. Tungsten(VI) chloride (WCl_6, ≥99.9%) was purchased from Sigma-Aldrich. Oxalic acid ($H_2C_2O_4$, anhydrous, 98%) was purchased from Alfa-Aesar. Chromium(III) nitrate nonahydrate ($Cr(NO_3)_3 \cdot 9H_2O$, 99%), iron(III) nitrate nonahydrate ($Fe(NO_3)_3 \cdot 6H_2O$, 99%), and nickel nitrate hexahydrate ($Ni(NO_3)_2 \cdot 6H_2O$, 99%) were obtained from Sigma-Aldrich. Ethyl alcohol (99.5%) was bought from Shimakyu's Pure Chemicals (Osaka, Japan).

2.2 Preparation of catalysts

2.2.1 Synthesis of WO_3. WO_3 was prepared *via* the solvothermal method following a literature report.[42] First, 0.4 g of WCl_6 was dissolved in 80 mL of ethanol. Subsequently, 4 g of oxalic acid was added to the solution, and the mixture was stirred until the solution became transparent. Then, the solution was transferred to a sealed 100 mL Teflon-lined stainless-steel autoclave and placed in an oven at 100 °C for 24 h. After the heating process, the autoclave was cooled naturally to room temperature. The WO_3 powders were then collected by centrifugation and washed three times with deionized (DI) water and absolute ethanol. Subsequently, the collected products were subjected to freeze-drying to prevent particle aggregation. Finally, the products were annealed at 165 °C under atmospheric conditions to enhance their crystallinity.

2.2.2 Synthesis of SA-M/WO_3 (M = Cr, Fe, and Ni). SA-M/WO_3 denotes single-atom-anchored WO_3, where M represents the transition metal that is anchored onto the WO_3 surface. SA-Fe/WO_3 was synthesized using the wet impregnation method.[43,44] Initially, 1 mmol $Fe(NO_3)_3 \cdot 9H_2O$ and 20 mL of ethanol were added to a flask. The solution was then bubbled with high-purity argon for 30 minutes to remove any dissolved gas. Then, 80 mg of the WO_3 powder was added to the solution and stirred to evenly disperse the powder. The solution was heated to 80 °C in an oil bath to facilitate the anchoring of Fe ions onto the surface of WO_3. For SA-Cr/WO_3 and SA-Ni/WO_3, the procedures were the same, with only the metal precursors changed to $Cr(NO_3)_3 \cdot 9H_2O$ and $Ni(NO_3)_2 \cdot 6H_2O$, respectively.

2.3 Material characterization

The crystal structure of the catalysts was analyzed using a powder X-ray diffractometer (XRD, Bruker, D2 Phaser) with Cu Kα radiation ($\lambda = 0.1540$ nm). The catalyst morphologies were studied using scanning electron microscopy (SEM, JEOL, JSM-6500), high-resolution transmission electron microscopy (HRTEM, JEOL JEM-2100F), and scanning transmission electron microscopy (STEM, JEOL, JEM-ARM300F2), operated at 200 kV. The surface areas of catalysts were studied by Brunauer–Emmett–Teller (BET) analysis (BELSORB MAX II). CO_2 adsorption behavior was determined using temperature-programmed desorption (TPD) measurements (AutoChem II 2920 Micrometrics). Light absorption measurements were performed by ultraviolet-visible-near infrared (UV-vis-NIR) spectroscopy (JASCO, V-670) with an integrated sphere using the $BaSO_4$ powder as the standard reference. Photoluminescence (PL) spectra were measured using a custom-built confocal fiber microscope integrated with a HORIBA iHR550 system, equipped with a Syncerity BI-NIR CCD camera (wavelength range: 400 to 1075 nm) and a diode laser (405 nm) as the excitation source. Time-resolved photoluminescence (TRPL) signals were collected using a photomultiplier detector (PicoQuant, PMA192, wavelength range: 230 to 920 nm). XPS was measured by an X-ray photoelectron spectroscopy system (ULVAC-PHI, PHI 5000 VersaProbe III) using monochromated Al Kα (1486.6 eV) X-ray as the excitation source. The XPS signals were calibrated to the C 1s peak at 284.6 eV. The elemental composition was measured by inductively coupled plasma optical emission spectroscopy (ICP-OES, Agilent 710-ES). X-ray absorption spectroscopy (XAS) data were acquired at the National Synchrotron Radiation Research Center (NSRRC, Hsinchu, Taiwan). The W L_3-edge was measured in the transmission mode at NSRRC TLS BL01 C1. The Cr K-edge, Fe K-edge and Ni K-edge spectra were collected in the fluorescence mode at NSRRC TPS BL44 A. The reaction intermediates formed during the photoreduction process were monitored using *in situ* FTIR spectroscopy (Bruker Tensor 27).[23,45,46]

2.4 Photocatalytic CO_2 reduction reaction

A batch-type photocatalytic CO_2 reduction experiment was conducted to investigate the performance of the photocatalyst. Prior to the photocatalytic CO_2 reduction test, 50 mg of the photocatalyst was placed in a homemade gas-tight quartz reactor with a 30 mL volume and evacuated to remove any air. The reactor was then filled with high-purity CO_2 (99.9999%), which passed through a water bubbler at a constant flow rate of 100 sccm for 30 minutes under atmospheric pressure. A 150 W AM1.5 solar simulator (Xe lamp) with an intensity of 100 mW cm^{-2} was used as the light source. After 4 h of light exposure, the photocatalytic products were analyzed by gas chromatography (GC, HP 6890 GC-HID) using a Shin-Carbon ST column for product separation. For the isotope test, $^{12}CO_2$ was replaced by $^{13}CO_2$, and the light exposure time was extended to 24 h. The photocatalytic products were analyzed by mass spectrometry (Agilent 7890 CB). The apparent quantum efficiency (AQE) is defined by the ratio of the effective electrons utilized in solar fuel production to the total photons incident on the catalyst. The AQE was calculated using the following equation:

$$\mathrm{AQE}(\%) = \frac{\text{number of electrons}}{\text{total photons incident on the catalyst}} \times 100\% = \frac{\alpha \times Y \times N}{\theta \times T \times S} \times 100\%, \quad (1)$$

where α represents the number of electrons involved in solar fuel formation ($\alpha_{CO} = 2$, $\alpha_{CH_4} = 8$, and $\alpha_{H_2} = 2$), Y is the yield of solar fuel products, N is the Avogadro number, θ is the photon flux, T is the irradiation time, and S is the irradiation area. To calculate the absorbed photon quantum efficiency (APQE), the total photons incident on the catalyst are replaced by the total photons absorbed ($\lambda < \lambda_g$) by the catalyst. In the case of SA-Fe–WO_3, $N = 6.022 \times 10^{23}$ mol^{-1}, $\theta = 2.58 \times 10^{17}$ s^{-1} cm^{-2} (integrated photon flux from 300 to 1100 nm), $T = 4$ h, and $S = 4$ cm^2. For APQE calculations, $\theta(\lambda < \lambda_g) = 8.86 \times 10^{15}$ s^{-1} cm^{-2} ($\lambda_g = 413$ nm).

2.5 Theoretical calculations

Spin-polarized DFT calculations were performed using the Vienna *ab initio* simulation package (VASP).[47] The projector-augmented wave (PAW) method was employed to describe core-valence interactions.[48] The exchange–correlation functional was treated within the generalized gradient approximation (GGA) using the Perdew–Burke–Ernzerhof (PBE) scheme.[49] A $2 \times 2 \times 4$ supercell of WO_3 (cubic phase, space group $Pm\bar{3}m$)

was constructed as the computational model. The plane-wave cutoff energy was set to 600 eV for all models. Valence electron configurations were $5d^5 6s^1$ for W, $2s^2 2p^4$ for O, $3d^5 4s^1$ for Cr, $3d^7 4s^1$ for Fe, and $3d^9 4s^1$ for Ni. A *k*-point convergence test was performed, leading to the selection of a $4 \times 4 \times 1$ *k*-point mesh, as shown in Fig. S1. Electronic and ionic relaxations were carried out with convergence criteria of 10^{-5} eV for energy and 0.005 eV $Å^{-1}$ for forces, respectively. To eliminate the interaction between periodic images, a vacuum space (>20 Å) was added in the *z*-direction.

The formation energy (ΔE_f) was calculated as follows:

$$\Delta E_f = E(\text{anchored } WO_3) - E(WO_3) - \sum_i n_i \mu_i, \quad (2)$$

where E(anchored WO_3) and $E(WO_3)$ represent the electronic energies of the WO_3 supercell with and without the metal dopant, respectively. n_i denotes the number of atoms added ($n_i > 0$) or removed ($n_i < 0$) relative to the WO_3 supercell, and μ_i is the chemical potential of the atom i, obtained from its pure metal phase. The CO_2 adsorption energy was calculated by taking the electronic energy of the system with CO_2 adsorbed and subtracting the combined electronic energy of the pristine surface and the energy of an isolated CO_2 molecule.

The Gibbs free energy was calculated by adding thermal corrections to the electronic energy, shown in eqn (3) (ref. 12 and 50–52) as follows:

$$G = E_{DFT} + ZPE + H_{(\vec{0}T)} - TS, \quad (3)$$

where E_{DFT} is the electronic energy. ZPE, $H_{(\vec{0}T)}$, and S represent the zero-point energy, enthalpy contribution, and entropy, respectively, obtained from vibrational frequency calculations. Only the vibrations of the active sites and adsorbates were considered, while the remaining catalyst atoms were assumed negligible and fixed at their optimized positions. T denotes the temperature, which was set to 300 K in all calculations. In the reaction pathway diagram, the free energy changes (ΔG) of intermediates were referenced to the free energies of a gas-phase CO_2 molecule, the clean surface, and half of the free energy of an H_2 molecule multiplied by the number of added hydrogen atoms.[12]

3 Results and discussion

To investigate the impact of the surface atomic structure and electron density distribution on the PC-CO_2RR, wet impregnation methods were employed to anchor the desired transition metals onto the surface of WO_3. This method enables the modification of the WO_3 surface while maintaining its crystalline structure and preserving its bulk properties. Hence, it hinders the PC-CO_2RR performance from being affected by other factors.

XRD and TEM analyses were conducted to confirm the crystal structure of the as-synthesized WO_3 and SA-M–WO_3 (M = Cr, Fe and Ni). As depicted in Fig. 1(a), the XRD patterns reveal that all the diffraction peaks of the as-synthesized WO_3 are consistent with those of cubic-phase WO_3. The TEM images

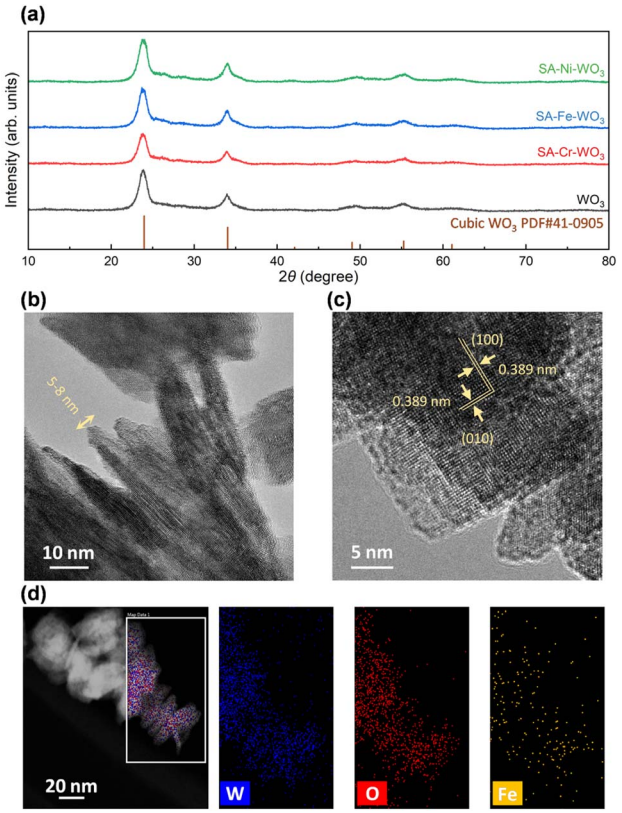

Fig. 1 Material characterizations. (a) XRD patterns of WO_3, SA-Cr–WO_3, SA-Fe–WO_3, and SA-Ni–WO_3. (b and c) HRTEM images of SA-Fe–WO_3 under different magnifications. (d) HAADF and EDS elemental mapping images of SA-Fe–WO_3.

illustrate a cubic nanoplate morphology for WO_3 with an average diameter of 50 nm and thicknesses ranging from 5 to 8 nm, which is beneficial for interlayer charge transfer (Fig. 1(b and c)). After the wet impregnation process, the XRD patterns of SA-Cr–WO_3, SA-Fe–WO_3, and SA-Ni–WO_3 are nearly identical to those of the as-synthesized WO_3. This indicates that no metal or metal oxide clusters are formed, and no metals are intercalated during the surface modification process. TEM and SEM images (Fig. S2 and S3) show no significant morphological changes. To evaluate surface area variations, BET analysis was performed, which revealed similar surface areas across all samples (Fig. S4). The results exhibit a typical type II isothermal curve with a type H3 hysteresis loop, characteristic of plate-like particle aggregation.[53] Additionally, UV-vis measurements were conducted to confirm light absorption properties, showing an absorption edge near 450 nm for all samples (Fig. S5).[54] Power-dependent PL analyses were also carried out to examine the light emission properties (Fig. S6). The results show that the intensity ratios of emission peaks E_A and E_B under different excitation powers (0.25 to 15.25 mW) are similar, implying that all the modified samples have optical properties similar to the pristine WO_3. Based on the above-mentioned observations, it can be concluded that the surface modification introduces new catalytically active sites without affecting the electronic structure, accessible surface area, or morphology of the WO_3 support. To

confirm the presence of anchored metals and their distributions, HRTEM, high-angle annular dark-field STEM, and energy-dispersive X-ray spectroscopy (EDS) elemental mapping images were recorded. As shown in Fig. 1(c), the interplanar spacing of SA-Fe–WO_3 nanoplates is 3.9 Å, corresponding to the (100) and (010) planes of cubic WO_3.[55,56] The observation of these mutually perpendicular lattice planes within the nanoplate confirms that the primary exposed surface (the basal plane) is the (001) facet. No additional metals or metal oxides are observed in the HRTEM images. Meanwhile, EDS elemental mapping images show that W, O and Fe are uniformly distributed over the WO_3 surface (Fig. 1(d)), confirming the presence of the atomically dispersed Fe on the WO_3 nanoplates. We observed the same for SA-Cr–WO_3 and SA-Ni–WO_3 (Fig. S7). Additionally, ICP-OES was performed to precisely determine the elemental composition of the materials (Table S1). The results indicate that the metal doping levels (*i.e.*, M/(W + O)) are approximately 1% for all samples.

To identify the chemical information and coordination environment of loaded metals (Cr, Fe and Ni) in the SA-M–WO_3 samples, XAS was employed to measure the K-edge of Cr, Fe and Ni, respectively (Fig. 2(a–c)). The X-ray absorption near-edge spectroscopy (XANES) spectra of all the Cr, Fe, and Ni K-edges exhibit noticeably different spectral curves compared with the standard metal foil reference. The prominent white line intensity in the Cr, Fe, and Ni K-edge spectra indicates that the loaded metals are in oxidized states rather than metallic states, implying the absence of metal clusters on the surface. However, their XANES spectra also slightly deviate from their typical metal oxide spectra. To further confirm the exact coordination environment of the loaded metal, the Fourier transforms of the Cr, Fe and Ni K-edge k^4-weighted extended X-ray absorption fine structures (EXAFS) were processed to acquire bond length information in the real (R) space. As shown in Fig. 2(d), the EXAFS spectra of SA-Cr–WO_3, SA-Fe–WO_3 and SA-Ni–WO_3 exhibit main peaks at 1.51, 1.52 and 1.57 Å, respectively, which are close to the bond length of the M–O bond in the first shell.[57–59] EXAFS fittings were also processed with the model of an anchored metal bonded to oxygen, which agrees well with the experimental results. The details of EXAFS fitting parameters are shown in Table S2. Moreover, no other extra peaks are found in the range from 2 to 4 Å, indicating that there are no M–M bonds or second shells of M–O–M bonds. This provides evidence that the loaded metals are atomically dispersed, isolated and bonded on the WO_3 surface.

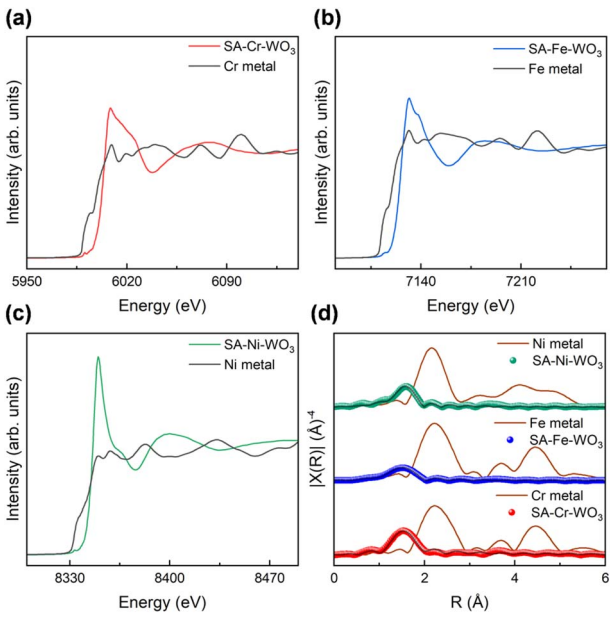

Fig. 2 Structural characterization of transition metal-anchored WO_3 by XAS. XANES spectra (fluorescence mode) of (a) SA-Cr–WO_3, (b) SA-Fe–WO_3, and (c) SA-Ni–WO_3. (d) FT-EXAFS fitting results of transition metal-anchored WO_3. The black line represents the fitting curve, while the brown line represents the standard metal reference.

XPS spectra were recorded to investigate the interaction between the loaded metals and WO_3, study the chemical compositions, and gain insights into the charge transfer behavior. The core-level spectra of the loaded metals were measured to confirm their successful incorporation onto the WO_3 surface (Fig. S8). The peak positions of these metals correspond to their oxide states, indicating bonding with surface oxygen, which is consistent with the XAS results. To further examine charge transfer behavior, the core levels of tungsten and oxygen were analyzed. As depicted in Fig. 3(a), the doublet peaks of W 4f in pristine WO_3 are observed at 37.5 eV (W $4f_{5/2}$) and 35.3 eV (W $4f_{7/2}$). In its O 1s spectra, pristine WO_3 also exhibits two peaks located at 530.7 eV and 532.5 eV, which are attributed to lattice oxygen and –OH, respectively.[60] It should be noted that the ratio of O to W matches the stoichiometric ratio (Table S3). After metal loading, both W 4f and O 1s peaks shift toward lower binding energies, indicating electron transfer from the loaded metals to WO_3. The shift in XPS signals follows the trend: SA-Fe–WO_3 > SA-Ni–WO_3 > SA–SA-Cr–WO_3 > WO_3, exhibiting a volcano plot behavior. Particularly, SA-Fe/WO_3 exhibits the most significant shift for W 4f from 35.3 to 35.2 eV and for O 1s from 530.7 to 530.5 eV, implying the strongest interaction between Fe atoms and WO_3, with more electrons transferred from Fe atoms to WO_3. Notably, O 1s displays a larger change because it is in the first shell of the doped metals. In addition, XAS measurements were conducted to elucidate the charge transfer behavior within the materials. The intensity of the white line in the L-edge spectrum is an indicator of d-orbital occupancy, *i.e.*, a lower edge intensity indicates higher d-orbital occupancy. The normalized W L_3-edge spectra are presented in Fig. 3(b). It can be observed that the intensity of the W L_3-edge decreases while the metals are loaded onto the WO_3, indicating a decrease in empty orbitals. It implies that introducing metals leads to charge transfer between loaded metals and WO_3. While the loaded metals provide excess electrons to fill the d-orbitals, the excited electrons are not allowed to process bound-state transitions (2p to 5d). Among all the samples, it is observed that SA-Fe–WO_3 exhibits the greatest decrease in white line intensity, indicating that the charge density transfer between Fe and WO_3 is the highest, while that between Cr and WO_3 is the lowest. This result is also consistent with the XPS results. Based on the

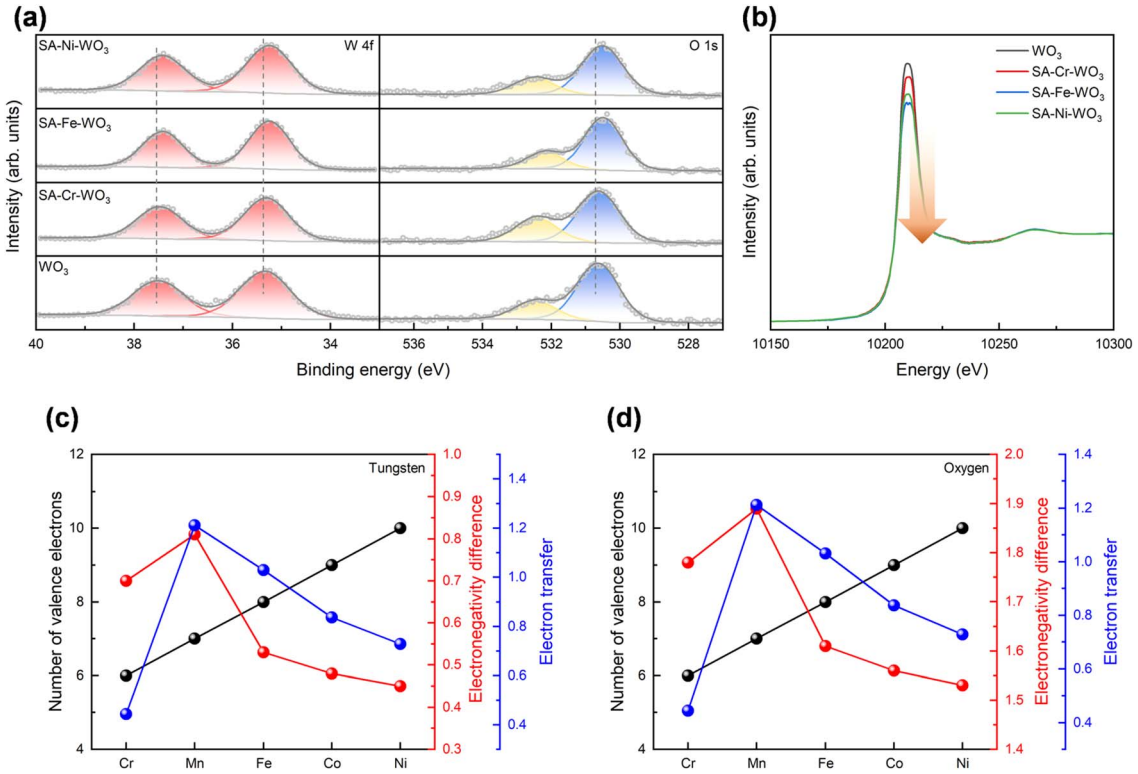

Fig. 3 Charge transfer analysis with different metal (Cr, Fe, and Ni) modifications. (a) W 4f and O 1s spectra of WO_3, SA-Cr–WO_3, SA-Fe–WO_3, and SA-Ni–WO_3. (b) XANES spectra (transmission mode) at the W L_3-edge for WO_3, Cr–WO_3, Fe–WO_3, and Ni–WO_3. (c and d) Relationship between the charge transfer, valence electrons and electronegativity of W and O elements, respectively. (Electron transfer is calculated from DFT).

initial material design principles, doped metal atoms with a higher number of valence electrons are more likely to donate electrons to the substrate material. Meanwhile, the electronegativity of the element influences the degree of electron transfer, as shown in Fig. 3(c and d). Hence, it can be concluded that Fe can be considered the single atom with the most electron density transfer to WO_3.

To study the impact of different metal loadings on the CO_2RR performance, we conducted a series of PC tests. For these tests, the materials were sealed in a batch-type quartz reactor filled with CO_2 and water vapor, followed by light irradiation for 4 h. As shown in Fig. 4(a), the main products for pristine WO_3 are CO, H_2, and CH_4, with yields of 4.5, 0.97, and 0.2 μmol g^{-1}, respectively. Doping with Cr, Fe, and Ni shows improvements in the product yields. Specifically, with Cr doping, the yields of CO, H_2, and CH_4 increase to 7, 1.3, and 0.7 μmol g^{-1}, respectively. Fe doping results in the highest increase in the yield among all three samples, with CO, H_2, and CH_4 yields reaching 12.1, 3.1, and 0.6 μmol g^{-1}, respectively, which are approximately three times higher than those of pristine WO_3. However, Ni doping leads to a modest increase in the yield, with CO, H_2, and CH_4 production falling to 8.9, 1.9, and 0.6 μmol g^{-1}, respectively. This volcano-like behavior is analogous to the degree of charge transfer observed (Fig. 4(a)). When the charge transfer within the material increases, the photocatalytic CO_2 reduction activity is also enhanced. This similar trend suggests a correlation between charge transfer and photocatalytic CO_2 reduction activity.

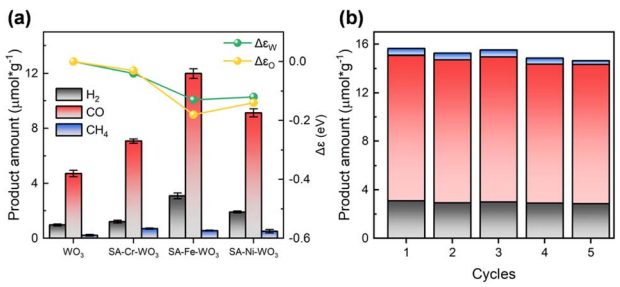

Fig. 4 Photocatalytic CO_2 reduction. (a) Average product yields of WO_3, SA-Cr–WO_3, SA-Fe–WO_3, and SA-Ni–WO_3 for an irradiation time of 4 h. W 4f and O 1s peak shifts from the XPS results are also included for the comparison. (b) Cycling stability test for SA-Fe–WO_3.

To determine the optimal catalyst configuration, a series of SA-Fe–WO_3 samples with varying Fe concentrations was systematically evaluated. The results indicate that the optimal loading amount is 1.0%, and the CO_2 reduction efficiency begins to decrease as the concentration is further increased to 1.5% (Fig. S9). This performance decline is attributed to the fact that high loading amounts facilitate the formation of metal clusters, which leads to the loss of the unique charge transfer behavior characteristic of isolated single atoms. Supporting this

conclusion, XPS results reveal that the 1.5% sample does not exhibit the significant binding energy shifts found at lower loadings, suggesting a lack of effective electronic interactions between the Fe species and the WO_3 support (Fig. S10).

To test the stability of the materials during the PC-CO_2RR experiment, the samples were recycled after each cycle of photocatalytic CO_2 reduction and then subjected to the same PC test. The results indicate that the samples maintain good stability after five cycles (~20 h). In addition, a blank test experiment was conducted to confirm that the CO_2RR products were indeed converted from CO_2 and not from surface contamination (Fig. S11). Isotope tracer analyses were also performed to understand the carbon source of products CO and CH_4 (Fig. S12). The overall AQE and APQE reach approximately 0.007% and 0.21%, respectively, which is in the range of the highest productivity plants that have a typical efficiency of about 1% annually.[61]

A superior CO_2RR performance is often accompanied by electron localization in the material, which is beneficial to CO_2 adsorption and activation.[13,15,16] Our results show a potential correlation between the charge transfer and CO_2RR activity. To address it in detail, we performed DFT calculations to investigate the impact of anchored Cr, Mn, Fe, Co and Ni atoms on the redistribution of the surface charge density and CO_2 adsorption over the WO_3 surface. According to the XRD and TEM results, the cubic WO_3 surface was cleaved along the (001) direction of bulk WO_3. A 2 × 2 × 4 supercell was then constructed as the computational model. Based on the XAS results, the doped metal coordinates with oxygen atoms, suggesting two possible anchoring configurations for Cr, Fe, and Ni: (I) the metal is positioned directly on an oxygen site ("M on O") or (II) the metal is surrounded by four oxygen atoms ("M anchored"). Formation energy calculations (Fig. S13) indicate that Cr, Fe, and Ni preferentially adopt the configuration anchored between four oxygen atoms (Fig. S14). The charge density differences were calculated to explore the redistribution of the charge density on the WO_3 surface. As displayed in Fig. 5, it is observed that electron accumulation occurs near the W and O atoms adjacent to the doped metals, *i.e.*, redistributing surface charge density or creating localized electron-rich regions, while electron depletion occurs at the doped metals. To further quantify the amount of transferred electrons from the anchored metals, Bader charge analysis was conducted.[62] The results clearly show that anchored Cr, Mn, Fe, Co and Ni can transfer 0.44, 1.21, 1.03, 0.84 and 0.73 e^- to the neighboring atoms, respectively, thereby enhancing the surface electron density. Specifically, the electron population of the neighboring W atoms increases from 3.45 e^- in pristine WO_3 to 3.47, 3.59, 3.58, 3.53 and 3.52 e^- for SA-Cr, SA-Mn, SA-Fe, SA-Co and SA-Ni, respectively. A similar trend is observed for the neighboring O atoms, where the electron population rises from 6.99 to 7.07, 7.14, 7.10, 7.11, and 7.08 e^-, respectively. This quantitative trend, summarized in Fig. S15 and Table S4, aligns perfectly with our XPS and XANES findings. The charge localization induced by Fe can be attributed to the ideal balance between its valence electron count and electronegativity (see Fig. 3(c and d)). While Cr has a relatively low electronegativity, its limited number of valence electrons ($3d^54s^1$) restricts the total amount of transferable charge. Conversely, although Ni possesses the highest valence electron count ($3d^94s^1$), its high electronegativity exerts a stronger pull on its electrons, thereby hindering effective transfer to the WO_3 substrate. Mn ($3d^54s^2$) and Fe ($3d^74s^1$) represent a synergistic optimum, providing a sufficient valence electron supply while maintaining a moderate electronegativity, which maximizes the localized surface charge density to promote CO_2 activation.

In addition, the next question would be "how does the position of the metal dopant influence the charge density distribution?". To address this question, we calculated the charge density distribution with the metals placed at various positions, as illustrated in Fig. S15. The results reveal minimal charge transfer when the metal substitutes at W sites. Furthermore, when the dopants occupy interstitial sites within the WO_3 lattice, the surface W atoms exhibit a tendency to lose electrons. This indicates that the surface assumes an electron-deficient character. Consequently, this suggests that only surface-anchored metals can effectively induce localized charge accumulation on the catalyst. However, substitutional and interstitial site doping are thermodynamically more stable than anchored doping, as shown in Fig. S16. Therefore, to promote metal anchoring on the catalyst surface and enhance kinetic feasibility, we employed a wet impregnation approach instead of *in situ* doping methods. Furthermore, considering that XPS analysis revealed the presence of surface hydroxyl groups (–OH), we constructed hydroxylated surface models (OH–WO_3 and SA-Fe–OH–WO_3) to evaluate the impact of –OH groups on the electronic environment. As summarized in Table S5, the introduction of surface –OH groups does not significantly alter the charge density of the surrounding W and O atoms. The consistent charge distribution between the pristine and hydroxylated surfaces confirms that the predictive selection

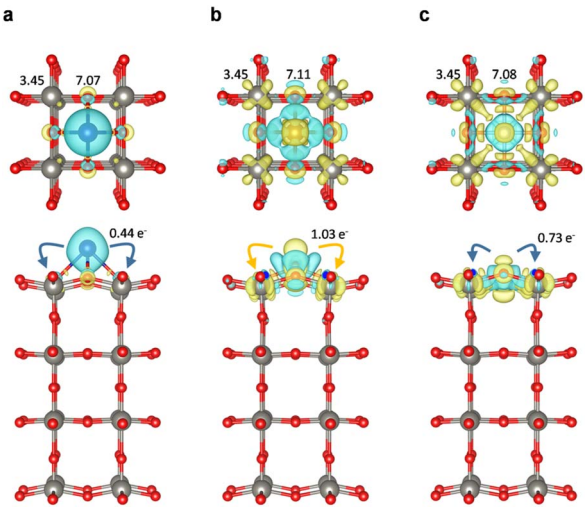

Fig. 5 Charge density distribution analyses of (a) SA-Cr–WO_3, (b) SA-Fe–WO_3 and (c) SA-Ni–WO_3 for charge densities with interface values of 0.003 e^- $Bohr^{-3}$. Yellow and cyan areas denote electron accumulation and depletion, respectively. Top: top view. Bottom: side view.

principle remains robust under realistic, hydrated reaction conditions.

To elucidate the role of the anchored metals in modulating CO_2 adsorption, we constructed CO_2 adsorption models to calculate the adsorption energy and associated charge transfer. Initially, several possible adsorption structures were optimized to identify the most stable CO_2 adsorption configurations. Their adsorption models and adsorption energies are shown in Fig. S17. The most stable configurations for CO_2 adsorbed on WO_3, SA-Cr–WO_3, SA-Mn–WO_3, SA-Fe–WO_3, SA-Co–WO_3, and SA-Ni–WO_3 are displayed in Fig. 6(a). The results indicate that CO_2 molecules can spontaneously adsorb onto all systems, as evidenced by negative adsorption energies. The transition metal-anchored samples exhibit stronger CO_2 adsorption than the pristine WO_3, as reflected by their more negative adsorption energies. The adsorption energy of CO_2 basically follows the trend of charge transfer: SA-Co–WO_3 ≈ SA-Mn–WO_3 > SA-Fe–WO_3 ≈ SA-Ni–WO_3 > SA-Cr–WO_3 > WO_3, suggesting that the increased localization of electrons enhances CO_2 adsorption. Specifically, CO_2 exhibits weaker interactions on pristine WO_3, with an adsorption energy of −0.33 eV, while SA-Cr–WO_3, SA-Mn–WO_3, SA-Fe–WO_3, SA-Co–WO_3 and SA-Ni–WO_3 show stronger interactions (mixed configuration) with adsorption energies of −0.41, −1.26, −1.01, −1.29 and −1.08 eV, respectively. In addition, SA-Fe–WO_3 exhibits another chemisorption mode of CO_2 (oxygen-down configuration) with an adsorption energy of −0.48 eV. Therefore, it is expected that the SA-Fe–WO_3 system has a higher possibility of adsorbing CO_2 for activation. Additionally, the configuration of adsorbed CO_2 serves as a crucial descriptor for high-performance catalysts, as the bond length and angle of the CO_2 molecule reflect its activation state.[63] In the pristine WO_3 system, CO_2 preferentially adsorbs on W and O sites, forming O–W and C–O bonds, respectively. However, the charge transfer from WO_3 to the CO_2 molecule is merely 0.01 electrons, and the CO_2 molecule remains in a nearly linear configuration (178.1°), characteristic of weak physical adsorption. In contrast, in SA-Cr–WO_3, SA-Mn–WO_3, SA-Fe–WO_3, SA-Co–WO_3 and SA-Ni–WO_3 systems, CO_2 preferentially coordinates with W and the anchored metal sites, forming O–W and C–M bonds, respectively, which induce CO_2 bending. The charge transfer from SA-Cr–WO_3, SA-Mn–WO_3, SA-Fe–WO_3, SA-Co–WO_3 and SA-Ni–WO_3 to the CO_2 molecule increases significantly, reaching 0.52, 0.71, 0.69, 0.64 and 0.53 electrons, respectively. Notably, in the oxygen-down configuration of SA-Fe–WO_3, charge transfer can reach up to 0.74 eV. As a result, the C=O bond length elongates from 1.18 Å to 1.26 Å, and the CO_2 molecular angle (∠O–C–O) reduces from 180° to 132.1°. More details are presented in Table S6. These results indicate that charge density localization enhances CO_2 adsorption and activation. To account for more realistic reaction conditions, the influence of surface hydroxylation on CO_2 adsorption was also systematically investigated. As summarized in Table S7, the adsorption energy of CO_2 on OH–WO_3 exhibits only a minor shift from −0.33 eV to −0.40 eV compared to the pristine surface. For the SA-Fe–OH–WO_3 system, although the presence of surface –OH groups leads to a slight decrease in adsorption strength (from −1.01 eV to −0.78 eV), the adsorption energy remains significantly more favorable than that of both pristine and hydroxylated WO_3 supports. These findings confirm that the Fe single-atom sites maintain their superior CO_2 activation capability even in a hydroxylated environment.

Furthermore, we confirmed the enhancement in CO_2 adsorption through TPD measurements. As shown in Fig. 6(b), the CO_2-TPD profile of the pristine WO_3 system exhibits a desorption peak near 50 °C, indicating the occurrence of physical adsorption. After anchoring Cr, Fe, and Ni, the desorption peaks shift to higher temperatures, with the SA-Fe–WO_3 system showing a prominent peak near 110 °C. This shift

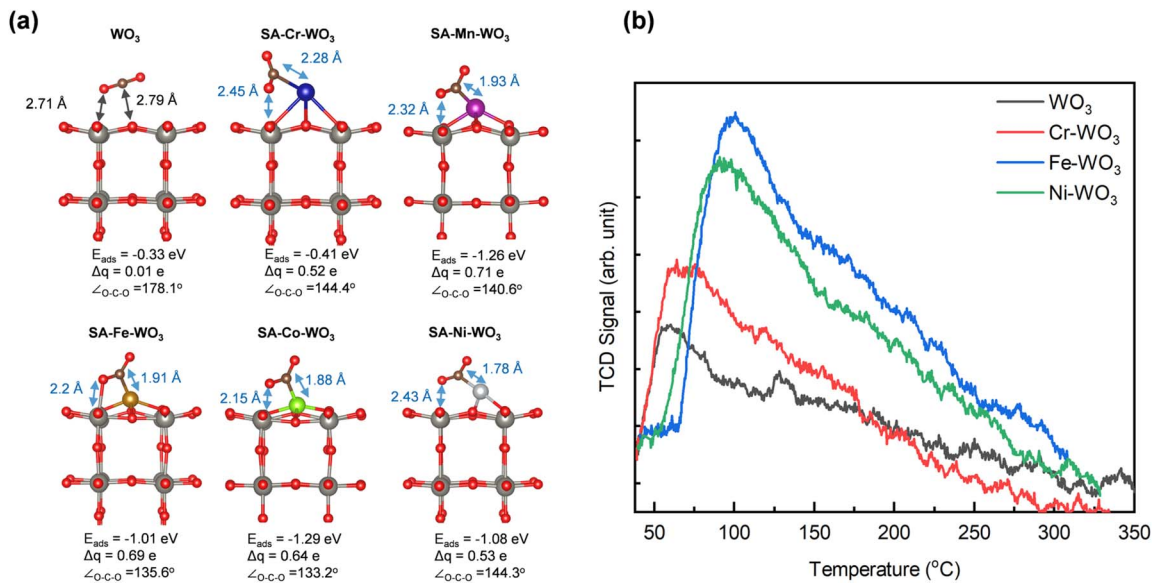

Fig. 6 CO_2 adsorption model and desorption behavior. (a) CO_2 adsorption models on WO_3, SA-Cr–WO_3, SA-Mn–WO_3, SA-Fe–WO_3, SA-Co–WO_3 and SA-Ni–WO_3. (b) CO_2-TPD profiles of the transition metal-anchored WO_3.

suggests the stronger chemisorption of CO_2 due to interactions with the anchored metal and tungsten. Additionally, a significant increase in the peak area is observed, which can be attributed to the two kinds of chemisorbed CO_2 species in the SA-Fe–WO_3 system. These experimental findings agree well with our simulation results. These results clearly reveal that the anchored metal modulates the surface charge density distribution of WO_3 to promote CO_2 activation. *In situ* FTIR spectroscopy was employed to elucidate the mechanistic pathway of the metal-anchored system during photocatalytic CO_2 reduction. *In situ* FTIR spectra show that several new characteristic peaks appear after purging CO_2 and H_2O vapor (Fig. 7(a), S18 and S19). The peak at 1695 cm^{-1} is assigned to the surface-adsorbed CO_2 (*CO_2), while the peaks at 1634 and 3421 cm^{-1} are attributed to the surface-adsorbed H_2O (H_2O*).[23,45,46] These results confirm that the essential reactants for the CO_2RR are successfully adsorbed on the catalyst surface prior to light irradiation. The peak intensities of *CO_2 and H_2O* increase during gas purging (Fig. 7(b)). Upon light irradiation, the intensities of the *CO_2 and H_2O* peaks decrease, signifying the consumption of the adsorbed species during the CO_2RR (Fig. 7(c), S18 and S19). This consumption is observed to be time-dependent, as the peak intensities continuously decrease over the irradiation period (Fig. 7(d)). The decreases in the peak intensities of *CO_2 and H_2O* obtained with the SA-Fe–WO_3 sample are 20% and 25% higher than those obtained with the pristine WO_3, highlighting that the enhanced reactivity of the SA-Fe–WO_3 sample could result from Fe anchoring. Notably, a new peak emerges at 1516 cm^{-1} after light irradiation, corresponding to the *COOH intermediate (Fig. 7(c)).[23,64,65] As noted in these references, this peak position is consistent with prior studies on metal oxide photocatalysts, where the characteristic bands of the *COOH species are typically observed in the 1500–1560 cm^{-1} region. For example, similar intermediate features have been reported at approximately 1536 cm^{-1} on Bi_2WO_6 surfaces.[23] The peak intensity of this intermediate is 40% greater on SA-Fe–WO_3 than on pristine WO_3, indicating that Fe anchoring enhances the formation of this key intermediate (Fig. 7(d)). This observation is consistent with our DFT calculations and TPD results. These results collectively demonstrate that anchoring Fe atoms significantly enhances

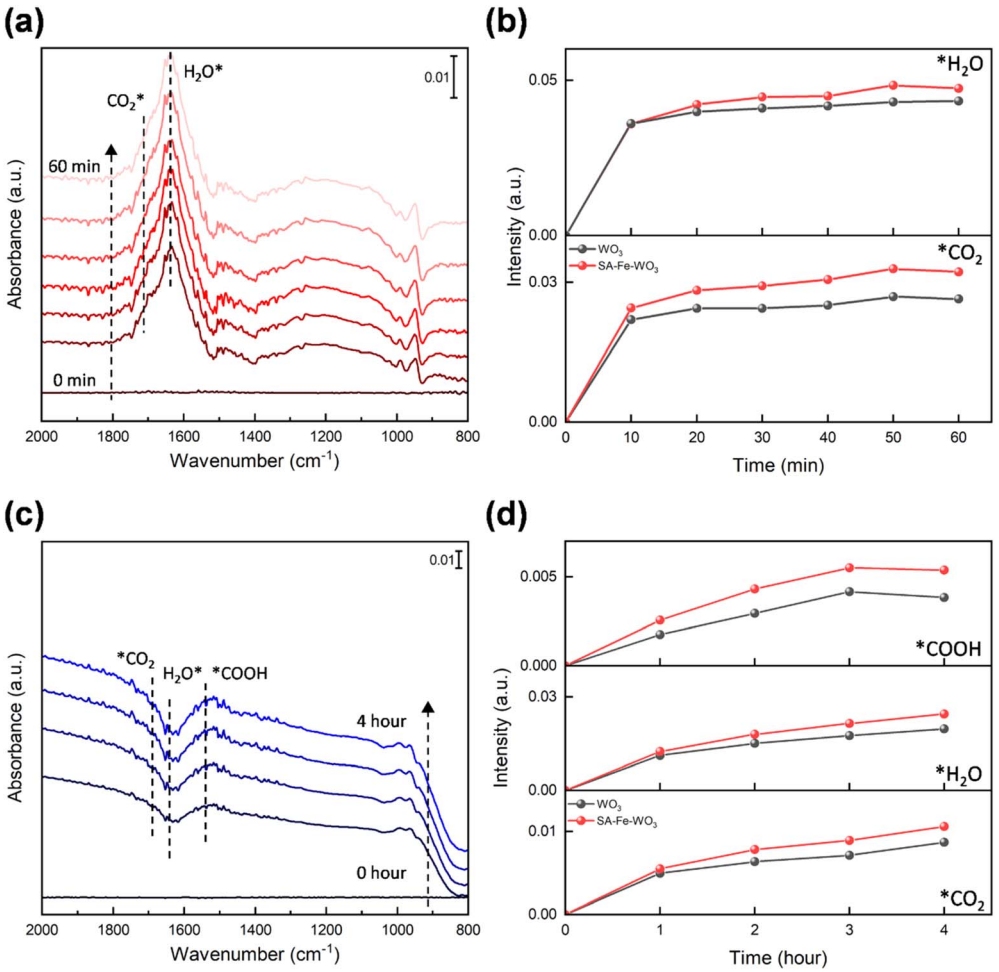

Fig. 7 *In situ* FTIR measurements. (a) *In situ* FTIR spectra of SA-Fe–WO_3 and (b) variation in IR peak intensities associated with *CO_2 and H_2O*, recorded in CO_2 and H_2O atmospheres under dark conditions. (c) *In situ* FTIR spectra of SA-Fe–WO_3 and (d) time-dependent variation in IR peak intensities associated with *CO_2, H_2O*, and the *COOH intermediate, recorded in H_2O and CO_2 atmospheres under light irradiation.

CO_2 activation and facilitates the subsequent formation of key intermediates in the photocatalytic pathway.

To further elucidate the origin of the enhanced photocatalytic activity in metal-anchored systems, Gibbs free energy calculations were conducted for the possible reaction pathways, guided by *in situ* FTIR observations of key intermediates. The detailed results are summarized in Fig. 8 and Tables S8–S13. Metal anchoring is found to significantly enhance CO_2 adsorption to form $*CO_2$, decreasing $\Delta G(*CO_2)$ from 0.16 eV for pristine WO_3 to 0.05 eV for SA-Cr–WO_3 and to negative values for SA-Fe–WO_3 (−0.53 eV) and SA-Ni–WO_3 (−0.54 eV), indicating a thermodynamically spontaneous process. This can be attributed to the stronger localized charge density introduced by the anchored metals, which effectively promotes CO_2 adsorption. In the subsequent protonation step, the formation of *COOH is identified as the possible rate-determining step (RDS) on

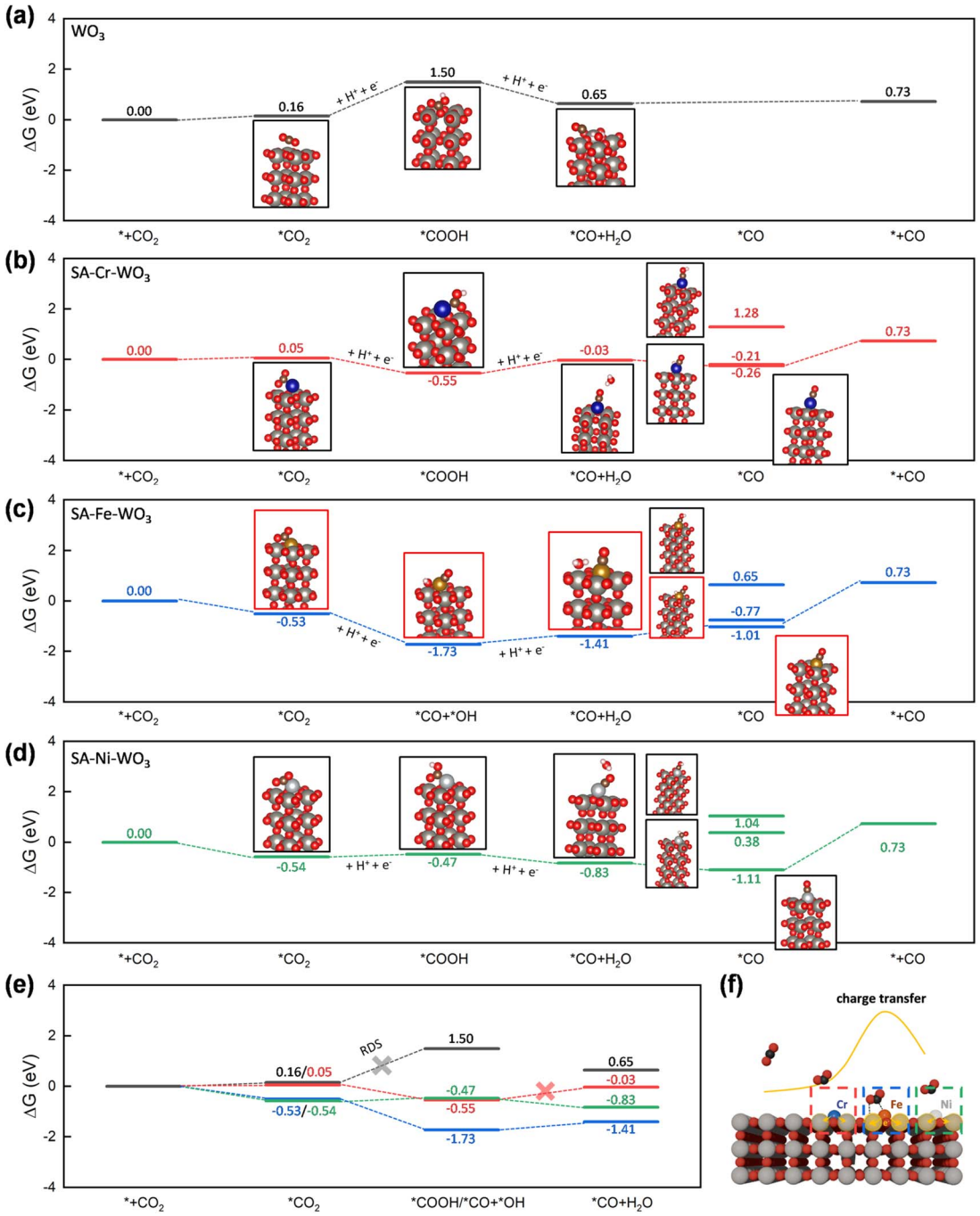

Fig. 8 Gibbs free energy calculation. Free energy diagrams for the photoreduction of CO_2 to CO over (a) pristine WO_3, (b) SA-Cr–WO_3, (c) SA-Fe–WO_3, and (d) SA-Ni–WO_3. (e) Key intermediate states involved in the CO_2-to-CO photoreduction pathway on WO_3, SA-Cr–WO_3, SA-Fe–WO_3, and SA-Ni–WO_3. (f) Schematic of the charge transfer over different single atoms and adsorbed CO_2.

pristine WO_3, with a high ΔG(*COOH) of 1.5 eV. In contrast, all metal-anchored systems render *COOH formation exothermic ($\Delta G < 0$), making the reaction thermodynamically favorable. Among them, the Fe-anchored system exhibits the most pronounced effect, with ΔG(*COOH) = −1.73 eV, consistent with the experimentally observed superior photocatalytic activity. SA-Cr–WO_3 and SA-Ni–WO_3 also facilitate COOH* formation, with ΔG(*COOH) of −0.47 eV and −0.55 eV, respectively. These results highlight that the stronger localized charge density not only enhances CO_2 adsorption but also stabilizes the first hydrogenated CO_2 intermediate. Notably, unlike other systems, SA-Fe–WO_3 spontaneously cleaves the C–OH bond in COOH*, forming *CO and *OH. Compared with the subsequent step of converting *COOH to *CO + H_2O, it can be inferred that the ease of *CO formation follows the order of SA-Fe–WO_3 > SA-Ni–WO_3 > SA-Cr–WO_3. SA-Ni–WO_3 exhibits a more favorable ΔG(*CO + H_2O) of −0.83 eV than SA-Cr–WO_3 (−0.03 eV), suggesting that the transformation of *COOH to CO is comparatively less favorable on SA-Cr–WO_3. This explains why the CO_2 conversion efficiency of SA-Ni–WO_3 is higher than that of SA-Cr–WO_3.

To further quantify the impact of charge accumulation on regulating the adsorption of *COOH, the adsorption energy and associated charge transfer were calculated and are summarized in Table S14. While *COOH adsorption is energetically unfavorable on pristine WO_3 with an adsorption energy of 0.51 eV, the introduction of single-atom sites dramatically stabilizes the intermediate, with the adsorption energy reaching −1.35 eV and −1.32 eV for SA-Cr–WO_3 and SA-Ni–WO_3, respectively. Structural parameters reveal that the O–C–OH bond angle of the adsorbed species on SACs decreases significantly to 115°, indicating a high degree of activation from the linear CO_2 geometry. Furthermore, Bader charge analysis confirms a substantial electron transfer to the *COOH moiety, reaching 1.62 electrons and 1.49 electrons for SA-Cr–WO_3 and SA-Ni–WO_3, respectively, which are significantly higher than the 0.47 e^- observed for pristine WO_3. This localized electron enrichment at the active site, driven by the synergistic interaction between the single atom and the WO_3 support, effectively weakens the C–OH bond and promotes COOH activation.

To further elucidate the product selectivity of CO, *COH and *CHO are also processed because both are critical intermediates for CH_4 formation. The Gibbs free energies (ΔG) for the formation of *COH on SA-Cr–WO_3 (1.28 eV), SA-Fe–WO_3 (0.65 eV), and SA-Ni–WO_3 (1.04 eV) are significantly higher than those for *CO formation. Similarly, the ΔG values for the formation of *CHO on SA-Cr–WO_3 (−0.21 eV) and SA-Ni–WO_3 (0.38 eV) are also higher than the energies associated with the *CO species formation. These elevated energy barriers indicate that further protonation of adsorbed *CO is thermodynamically unfavorable on the SA-M–WO_3 surfaces. Notably, on the SA-Fe–WO_3 catalyst, the CO–H bond in the potential *CHO intermediates undergoes spontaneous cleavage, which effectively terminates the pathway toward the formation of CH_4. These findings suggest that while the localized charge successfully stabilizes the initial *COOH intermediate, the specific electronic environment of the single-atom sites does not support the subsequent hydrogenation steps required for CH_4 production. Consequently, the catalysts exhibit high selectivity for CO desorption over further reduction because the energy required to reach the CH_4 intermediate is significantly higher.

The superior performance of SA-Fe–WO_3 is attributed to the maximal electron transfer from Fe to the WO_3 framework, as evidenced by the most significant shifts in XPS binding energies and W L_3-edge XANES intensities. Bader charge analysis confirms that Fe induces the highest localized charge accumulation at neighboring atoms compared to Cr and Ni, which stems from the optimal balance between its valence electron count and electronegativity. This enhanced surface charge localization promotes CO_2 activation and significantly stabilizes the key *COOH intermediate by lowering its formation energy. Collectively, these synergistic electronic factors lower the overall reaction barrier, leading to the observed threefold enhancement in photocatalytic CO_2 reduction efficiency.

4 Conclusions

In summary, single-atom-anchored WO_3 photocatalysts (SA-Cr–WO_3, SA-Fe–WO_3, and SA-Ni–WO_3) are successfully synthesized *via* the wet impregnation method, with the uniform dispersion of metals confirmed by EXAFS analysis. The anchored metals induce a redistribution of charge density, as supported by experiments (XPS and XAS) and DFT calculations. We observed that the anchored metals donate electrons to surrounding atoms, leading to localized charge density accumulation. This results in enhanced CO_2 molecule chemisorption, as demonstrated by TPD and DFT analyses. Moreover, Gibbs free energy calculations and *in situ* FTIR spectroscopy reveal that *COOH is the key intermediate, and metal anchoring lowers its activation barrier, rendering the reaction thermodynamically spontaneous. Stronger charge-density localization not only enhances CO_2 chemisorption but also promotes CO_2 activation. Consequently, the photocatalytic CO_2 reduction reaction performance is improved by three times with a yield of 12.1 μmol g^{-1} per 4 h (or APQE = 0.21%) for the CO product. These findings illustrate a strong correlation between charge density localization, CO_2 adsorption, and CO_2 activation and provide valuable insights for designing improved catalyst surfaces.

Author contributions

C.-Y. H. contributed to the idea, investigation, methodology, experiment, visualization, simulation and writing of the original draft. Y.-R. L. and M. H. assisted the simulation. M. E. A. performed the BET experiments. Y.-F. H. contributed to the conceptualization. T.-Y. L., K. L. and H.-L. W. performed the *in situ* FTIR experiments. K.-H. C. and L.-C. C. acquired the funding. M. Q., K.-H. C. and L.-C. C. supervised the project and reviewed and edited the manuscript.

Conflicts of interest

The authors declare no competing financial interests.

Data availability

The data supporting this article have been included as part of the supplementary information (SI). Supplementary information: Fig. S1–S19 and Tables S1–S14. See DOI: https://doi.org/10.1039/d5ta10187e.

Acknowledgements

This research was financially supported by the National Science and Technology Council (NSTC) in Taiwan under the Academic Summit Project (NSTC 112-2639-M-002-005-ASP, NSTC 113-2639-M-002-004-ASP and NSTC 114-2639-M-002-003-ASP), NSTC 111-2112-M-131-002-MY3 and NSTC 111-2112-M-019-006-MY3, as well as the Center of Atomic Initiative for New Materials (AI-Mat), the National Taiwan University [111 L9008, 112 L9008, 113 L9008 and 114 L9008], from the Featured Areas Research Center Program within the framework of the Higher Education Sprout Project by the Ministry of Education (MOE) of Taiwan. M.Q. acknowledges support from the National Science and Technology Council (NSTC) Taiwan [grant number: 114-2112-M-003-019-MY2]. In addition, we would like to thank Ms. C.-Y. Chien of the Ministry of Science and Technology (the National Taiwan University) for the assistance in the TEM experiments. The technical support from the Advanced Materials Characterization Lab, the Institute of Atomic and Molecular Sciences (IAMS), Academia Sinica, is also gratefully acknowledged. We also acknowledge the National Synchrotron Radiation Research Center (NSRRC) TLS 01C1 and TPS 44A for the assistance in XAS measurements. We are grateful to the Computer and Information Networking Center, the National Taiwan University for the support of the high-performance computing facilities.

References

1 Q. Yi, W. Li, J. Feng and K. Xie, *Chem. Soc. Rev.*, 2015, **44**, 5409–5445.
2 S. Solomon, G.-K. Plattner, R. Knutti and P. Friedlingstein, *Proc. Natl. Acad. Sci. U. S. A.*, 2009, **106**, 1704–1709.
3 J. Fu, K. Jiang, X. Qiu, J. Yu and M. Liu, *Mater. Today*, 2020, **32**, 222–243.
4 M. Aresta, A. Dibenedetto and A. Angelini, *Chem. Rev.*, 2014, **114**, 1709–1742.
5 S. Fang, M. Rahaman, J. Bharti, E. Reisner, M. Robert, G. A. Ozin and Y. H. Hu, *Nat. Rev. Methods Primers*, 2023, **3**, 61.
6 P.-P. Huang, M. Qorbani, Y.-T. Hung, Y.-R. Lai, A. Sabbah, M.-F. Tseng, C.-Y. Huang, S. Koodathil, S. Kholimatussadiah, M. K. Hussien, T.-H. Feng, Y.-H. Liu, H. Wang, J.-W. Lin, C.-H. Wang, C.-I. Wu, M. Hayashi, K.-H. Chen and L.-C. Chen, *ACS Nano*, 2026, **20**, 2211–2224.
7 Z. Sun, T. Ma, H. Tao, Q. Fan and B. Han, *Chem*, 2017, **3**, 560–587.
8 B. Han, X. Ou, Z. Deng, Y. Song, C. Tian, H. Deng, Y. J. Xu and Z. Lin, *Angew. Chem., Int. Ed.*, 2018, **57**, 16811–16815.
9 W. Yao, B. Wu and Y. Liu, *ACS Nano*, 2020, **14**, 9320–9346.
10 M. Qorbani, A. Sabbah, Y.-R. Lai, S. Kholimatussadiah, S. Quadir, C.-Y. Huang, I. Shown, Y.-F. Huang, M. Hayashi, K.-H. Chen and L.-C. Chen, *Nat. Commun.*, 2022, **13**, 1256.
11 W. Jiang, H. Loh, B. Q. L. Low, H. Zhu, J. Low, J. Z. X. Heng, K. Y. Tang, Z. Li, X. J. Loh and E. Ye, *Appl. Catal., B*, 2023, **321**, 122079.
12 X. Li, Y. Sun, J. Xu, Y. Shao, J. Wu, X. Xu, Y. Pan, H. Ju, J. Zhu and Y. Xie, *Nat. Energy*, 2019, **4**, 690–699.
13 Y. Cao, L. Guo, M. Dan, D. E. Doronkin, C. Han, Z. Rao, Y. Liu, J. Meng, Z. Huang and K. Zheng, *Nat. Commun.*, 2021, **12**, 1675.
14 J. Ji, R. Li, H. Zhang, Y. Duan, Q. Liu, H. Wang and Z. Shen, *Appl. Catal., B*, 2023, **321**, 122020.
15 Y. Wang, C. Ban, J. Meng, J. Ma, H. Zou, Y. Feng, J. Ding, Y. Duan, L. Gan and X. Zhou, *Sep. Purif. Technol.*, 2023, **312**, 123379.
16 H. M. Ngo, U. Pal, Y. S. Kang and K. M. Ok, *ACS Omega*, 2023, **8**, 8876–8884.
17 X. Jiao, X. Li, X. Jin, Y. Sun, J. Xu, L. Liang, H. Ju, J. Zhu, Y. Pan, W. Yan, Y. Lin and Y. Xie, *J. Am. Chem. Soc.*, 2017, **139**, 18044–18051.
18 A. Ñlvarez, M. Borges, J. J. Corral-Pérez, J. G. Olcina, L. Hu, D. Cornu, R. Huang, D. Stoian and A. Urakawa, *ChemPhysChem*, 2017, **18**, 3135–3141.
19 M. Pérez-Jiménez, H. Corona, F. De La Cruz-Martínez and J. Campos, *Chem.–Eur. J.*, 2023, **29**, e202301428.
20 A. M. Appel, J. E. Bercaw, A. B. Bocarsly, H. Dobbek, D. L. Dubois, M. Dupuis, J. G. Ferry, E. Fujita, R. Hille, P. J. Kenis, C. A. Kerfeld, R. H. Morris, C. H. F. Peden, A. R. Portis, S. W. Ragsdale, T. B. Rauchfuss, J. N. H. Reek, L. C. Seefeldt, R. K. Thauer and G. L. Waldrop, *Chem. Rev.*, 2013, **113**, 6621–6658.
21 X. Jin, Y. Xu, X. Zhou, C. Lv, Q. Huang, G. Chen, H. Xie, T. Ge, J. Cao, J. Zhan and L. Ye, *ACS Mater. Lett.*, 2021, **3**, 364–371.
22 M. K. Hussien, A. Sabbah, M. Qorbani, R. Putikam, S. Kholimatussadiah, D. L. M. Tzou, M. H. Elsayed, Y. J. Lu, Y. Y. Wang, X. H. Lee, T.-Y. Lin, N. Q. Thang, H.-L. Wu, S.-C. Haw, K. C.-W. Wu, M.-C. Lin, K.-H. Chen and L.-C. Chen, *Small*, 2024, 2400724.
23 N. Q. Thang, A. Sabbah, R. Putikam, C. Y. Huang, T. Y. Lin, M. K. Hussien, H. L. Wu, M. C. Lin, C. H. Lee, K. H. Chen and L.-C. Chen, *Adv. Funct. Mater.*, 2025, 2423751.
24 T. T. Mamo, M. Qorbani, A. G. Hailemariam, R. Putikam, C.-M. Chu, T.-R. Ko, A. Sabbah, C.-Y. Huang, S. Kholimatussadiah, T. Billo, M. K. Hussien, S.-Y. Chang, M.-C. Lin, W.-Y. Woon, H.-L. Wu, K.-T. Wong, L.-C. Chen and K.-H. Chen, *Nano Energy*, 2024, **128**, 109863.
25 S.-M. Chang and W.-S. Liu, *Appl. Catal., B*, 2011, **101**, 333–342.
26 H. Pan, M. Sun, X. Wang, M. Zhang, M. Murugananthan and Y. Zhang, *Appl. Catal., B*, 2022, **307**, 121174.
27 J. Li, M. Zhang, Z. Guan, Q. Li, C. He and J. Yang, *Appl. Catal., B*, 2017, **206**, 300–307.
28 Y. Pan, X. Wang, W. Zhang, L. Tang, Z. Mu, C. Liu, B. Tian, M. Fei, Y. Sun and H. Su, *Nat. Commun.*, 2022, **13**, 3063.
29 Z. Zhang, C. Feng, D. Wang, S. Zhou, R. Wang, S. Hu, H. Li, M. Zuo, Y. Kong and J. Bao, *Nat. Commun.*, 2022, **13**, 2473.

30 Y. Zhang, J. Zhao, H. Wang, B. Xiao, W. Zhang, X. Zhao, T. Lv, M. Thangamuthu, J. Zhang and Y. Guo, *Nat. Commun.*, 2022, **13**, 58.
31 W. Tu, Y. Xu, J. Wang, B. Zhang, T. Zhou, S. Yin, S. Wu, C. Li, Y. Huang, Y. Zhou, Z. Zou, J. Robertson, M. Kraft and R. Xu, *ACS Sustain. Chem. Eng.*, 2017, **5**, 7260–7268.
32 Y. An, H. L. Li, Y. Y. Liu, B. B. Huang, Q. L. Sun, Y. Dai, X. Y. Qin and X. Y. Zhang, *J. Solid State Chem.*, 2016, **233**, 194–198.
33 J. Yang, W. H. Li, K. Xu, S. Tan, D. Wang and Y. Li, *Angew Chem. Int. Ed. Engl.*, 2022, **61**, e202200366.
34 G. Wei, Z. Mao, L. Liu, T. Hao, L. Zhu, S. Xu, X. Wang and S. Tang, *ACS Appl. Mater. Interfaces*, 2024, **16**, 52233–52243.
35 Y. Q. Zhang, D. Wang, G. P. Wei, B. L. Li, Z. C. Mao, S. M. Xu, S. B. Tang, J. Jiang, Z. Y. Li, X. J. Wang and X. Xu, *JACS Au*, 2024, **4**, 1509–1520.
36 B. Hu, Z. Li, B. Wang, L. Chen, X. Wang, X. Hu, Z. Bai, Y. Li, G. Chen, X. Luo and S.-F. Yin, *Appl. Catal., B*, 2025, **371**, 125196.
37 H. Shi, H. Wang, Y. Zhou, J. Li, P. Zhai, X. Li, G. G. Gurzadyan, J. Hou, H. Yang and X. Guo, *Angew. Chem.*, 2022, **134**, e202208904.
38 P. Dong, G. Hou, X. Xi, R. Shao and F. Dong, *Environ. Sci.: Nano*, 2017, **4**, 539–557.
39 V. Dutta, S. Sharma, P. Raizada, V. K. Thakur, A. a. P. Khan, V. Saini, A. M. Asiri and P. Singh, *J. Environ. Chem. Eng.*, 2021, **9**, 105018.
40 X. Zhang, H. Su, P. Cui, Y. Cao, Z. Teng, Q. Zhang, Y. Wang, Y. Feng, R. Feng and J. Hou, *Nat. Commun.*, 2023, **14**, 7115.
41 S. H. Talib, S. Hussain, S. Baskaran, Z. Lu and J. Li, *ACS Catal.*, 2020, **10**, 11951–11961.
42 L. Liang, X. Li, Y. Sun, Y. Tan, X. Jiao, H. Ju, Z. Qi, J. Zhu and Y. Xie, *Joule*, 2018, **2**, 1004–1016.
43 J. Guo, H. Liu, D. Li, J. Wang, X. Djitcheu, D. He and Q. Zhang, *RSC Adv.*, 2022, **12**, 9373–9394.
44 H. Zhang, Y. Wang, S. Zuo, W. Zhou, J. Zhang and X. W. D. Lou, *J. Am. Chem. Soc.*, 2021, **143**, 2173–2177.
45 A. Sabbah, I. Shown, M. Qorbani, F.-Y. Fu, T.-Y. Lin, H.-L. Wu, P.-W. Chung, C.-I. Wu, S. R. M. Santiago, J.-L. Shen, K.-H. Chen and L.-C. Chen, *Nano Energy*, 2022, **93**, 106809.
46 F.-Y. Fu, C.-C. Fan, M. Qorbani, C.-Y. Huang, P.-C. Kuo, J.-S. Hwang, G.-J. Shu, S.-M. Chang, H.-L. Wu, C.-I. Wu, K.-H. Chen and L.-C. Chen, *Sustainable Energy Fuels*, 2022, **6**, 4418–4428.
47 G. Kresse and J. Furthmüller, *Phys. Rev. B: Condens. Matter Mater. Phys.*, 1996, **54**, 11169.
48 G. Kresse and D. Joubert, *Phys. Rev. B: Condens. Matter Mater. Phys.*, 1999, **59**, 1758.
49 J. P. Perdew, K. Burke and M. Ernzerhof, *Phys. Rev. Lett.*, 1996, **77**, 3865.
50 J. K. Nørskov, J. Rossmeisl, A. Logadottir, L. Lindqvist, J. R. Kitchin, T. Bligaard and H. Jonsson, *J. Phys. Chem. B*, 2004, **108**, 17886–17892.
51 L. I. Bendavid and E. A. Carter, *J. Phys. Chem. C*, 2013, **117**, 26048–26059.
52 V. Wang, N. Xu, J.-C. Liu, G. Tang and W.-T. Geng, *Comput. Phys. Commun.*, 2021, **267**, 108033.
53 M. Thommes, K. Kaneko, A. V. Neimark, J. P. Olivier, F. Rodriguez-Reinoso, J. Rouquerol and K. S. Sing, *Pure Appl. Chem.*, 2015, **87**, 1051–1069.
54 J. Klein, L. Kampermann, B. Mockenhaupt, M. Behrens, J. Strunk and G. Bacher, *Adv. Funct. Mater.*, 2023, **33**, 2304523.
55 H. Yang, H. Sun, Q. Li, P. Li, K. Song, B. Song and L. Wang, *Vacuum*, 2019, **164**, 411–420.
56 M. Gillet, K. Aguir, C. Lemire, E. Gillet and K. Schierbaum, *Thin Solid Films*, 2004, **467**, 239–246.
57 A. Boubnov, A. Roppertz, M. D. Kundrat, S. Mangold, B. Reznik, C. R. Jacob, S. Kureti and J.-D. Grunwaldt, *Appl. Surf. Sci.*, 2016, **386**, 234–246.
58 K. Pandya, W. O'grady, D. Corrigan, J. Mcbreen and R. Hoffman, *J. Phys. Chem.*, 1990, **94**, 21–26.
59 C. Zhong, Y. Xu, X. Wu, S. Yin, X. Zhang, L. Zhou and H. You, *Adv. Mater.*, 2024, **36**, 2309500.
60 T. J. Frankcombe and Y. Liu, *Chem. Mater.*, 2023, **35**, 5468–5474.
61 D. K. Dogutan and D. G. Nocera, *Accounts Chem. Res.*, 2019, **52**, 3143–3148.
62 W. Tang, E. Sanville and G. Henkelman, *J. Phys.: Condens. Matter*, 2009, **21**, 084204.
63 B. M. Abraham, O. Piqué, M. A. Khan, F. Viñes, F. Illas and J. K. Singh, *ACS Appl. Mater. Interfaces*, 2023, **15**, 30117–30126.
64 X. Li, Y. Li, P. Li, D. Yuan, Y. Fu, J. Huang, Y. Fang, F. Wang, M. Anpo and L. Tan, *Mol. Catal.*, 2025, **585**, 115356.
65 J. D. Yi, R. Xie, Z. L. Xie, G. L. Chai, T. F. Liu, R. P. Chen, Y. B. Huang and R. Cao, *Angew. Chem.*, 2020, **132**, 23849–23856.